

Current Biology

Maintaining symmetry during body axis elongation

Highlights

- A new role for the terminal patterning system in the fly embryo is reported
- Localized ERK signaling ensures bilateral symmetry during body axis elongation
- Reduced ERK signaling causes random helical twisting during axis elongation
- ERK works, at least in part, by controlling a locally expressed integrin receptor

Authors

Celia M. Smits, Sayantan Dutta, Vishank Jain-Sharma, Sebastian J. Streichan, Stanislav Y. Shvartsman

Correspondence

stas@princeton.edu

In brief

Smits et al. explore how bilateral symmetry is maintained during the movements of gastrulation in the developing *Drosophila melanogaster* embryo. Tissue mechanics associated with movement of the posterior midgut invagination and patterned by the terminal patterning system are found to be important to suppress asymmetrical movements.



Report

Maintaining symmetry during body axis elongation

Celia M. Smits,^{1,2} Sayantan Dutta,^{2,3} Vishank Jain-Sharma,⁴ Sebastian J. Streichan,^{4,5} and Stanislav Y. Shvartsman^{1,2,6,7,*}¹Department of Molecular Biology, Princeton University, Princeton, NJ 08544, USA²The Lewis-Sigler Institute for Integrative Genomics, Princeton University, Princeton, NJ 08544, USA³Department of Chemical and Biological Engineering, Princeton University, Princeton, NJ 08544, USA⁴Department of Physics, University of California, Santa Barbara, Santa Barbara, CA 93106, USA⁵Biomolecular Science and Engineering, University of California, Santa Barbara, Santa Barbara, CA 93106, USA⁶Center for Computational Biology, Flatiron Institute, Simons Foundation, New York, NY 10010, USA⁷Lead contact*Correspondence: stas@princeton.edu<https://doi.org/10.1016/j.cub.2023.07.050>

SUMMARY

Bilateral symmetry defines much of the animal kingdom and is crucial for numerous functions of bilaterian organisms. Genetic approaches have discovered highly conserved patterning networks that establish bilateral symmetry in early embryos,¹ but how this symmetry is maintained throughout subsequent morphogenetic events remains largely unknown.² Here we show that the terminal patterning system—which relies on Ras/ERK signaling through activation of the Torso receptor by its ligand Trunk³—is critical for preserving bilateral symmetry during *Drosophila* body axis elongation, a process driven by cell rearrangements in the two identical lateral regions of the embryo and specified by the dorsal-ventral and anterior-posterior patterning systems.⁴ We demonstrate that fluctuating asymmetries in this rapid convergent-extension process are attenuated in normal embryos over time, possibly through noise-dissipating forces from the posterior midgut invagination and movement. However, when Torso signaling is attenuated via mutation of Trunk or RNAi directed against downstream Ras/ERK pathway components, body axis elongation results in a characteristic corkscrew phenotype,⁵ which reflects dramatic reorganization of global tissue flow and is incompatible with viability. Our results reveal a new function downstream of the *Drosophila* terminal patterning system in potentially active control of bilateral symmetry and should motivate systematic search for similar symmetry-preserving regulatory mechanisms in other bilaterians.

RESULTS AND DISCUSSION

Bilateral symmetry in *Drosophila* is genetically established by the deposited mRNA and proteins that define the orthogonal anterior-posterior (AP) axis and dorsal-ventral (DV) axis of the embryo.^{6,7} A third bilaterally symmetrical system, terminal patterning, is active in the anterior and posterior poles of the embryo in a cap-like pattern.³ Guided by this genetic patterning information, the morphogenetic movements of gastrulation proceed stereotypically^{8,9}: first, the ventral furrow invaginates and cells on either side adhere to form a sealed midline, a morphological landmark for bilateral symmetry that persists through embryogenesis (Figure 1A, left). The two lateral germband tissues start convergence (along the DV axis) and extension (along the AP axis), driven by cell intercalations (Figure 1A, middle). Simultaneously, the posterior midgut (PMG) invaginates at the posterior-dorsal tip of the embryo, then moves anteriorly along with the extending germband (Figure 1A, right). This movement occurs in a planar fashion, such that the midline of the extending tissue lies parallel to the AP axis of the embryo, and both the left and right sides of the embryo are the same size (Video S1; Figure 1B). Here we show that this planar movement of the midline is actively maintained by downstream components of terminal patterning and is necessary for proper embryogenesis.

Bilateral symmetry is broken in mutants that exhibit the “corkscrew” phenotype, where the embryo twists into a helix, while the rest of the tissue seems to remain morphologically intact. One “class” of mutants that display this phenotype is in genes associated with PMG formation and propagation, including *scab* (*scb*), the mutants of which have been shown to twist during gastrulation.^{10–12} The second class of mutations are in positive regulators of the Ras pathway, including *csw* (for which the phenotype was named).⁵ We found that RNAi directed against KSR, a scaffolding protein and necessary positive downstream effector of Ras signaling, also produces a twisting phenotype¹³ (Table S1; Video S2). This led us to investigate the roles of terminal patterning and PMG formation in active maintenance of bilateral symmetry during gastrulation.

Terminal patterning is required for bilateral symmetry maintenance

Two of the previously identified mutants that form a twisted larval cuticle (*csw* and *ksr* RNAi) are positive regulators of the Ras pathway^{5,13} (Figure 1C, left), indicating that Ras signaling is important for maintaining symmetry during extension. Two instances of Ras pathway activation in the early embryo are affected by these mutations: one is the terminal patterning system, through activation of the receptor tyrosine kinase Torso in

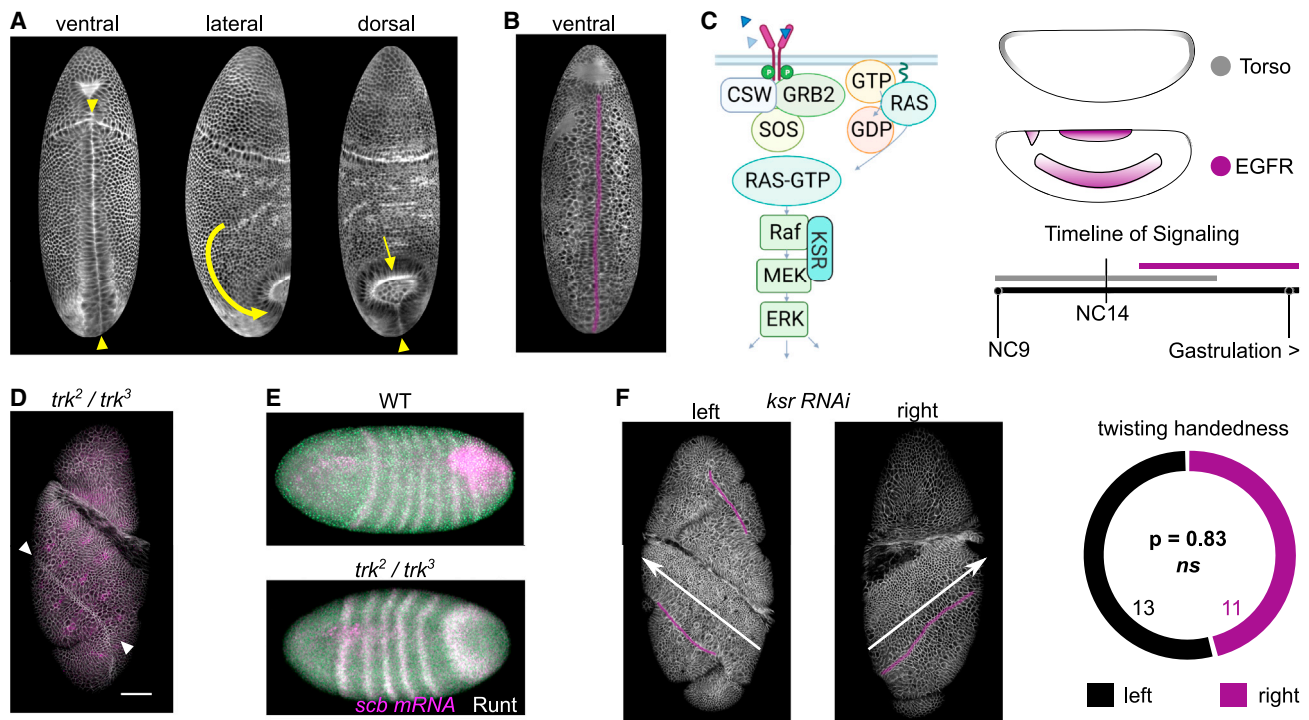


Figure 1. Loss of symmetry is downstream of terminal patterning

(A) Embryo depicting midline formation on the ventral side (left; midline, yellow arrows), germband extension on the lateral side (middle; tissue flow, arrow), and PMG formation on the dorsal side (PMG, arrow; midline, arrowhead). Each image is rotated 90° from the previous image. (B) Embryo at the end of germband extension; midline is highlighted (purple). (C) Left: schematic of the Ras/ERK pathway. Right: receptors upstream of Ras/ERK signaling in the early *Drosophila* embryo: Torso (gray) and EGFR (purple). Top shows spatial pattern of activation; bottom shows timeline and duration of pathway activity. (D) A *trk2/trk3* embryo fixed and stained for membranes (neurotactin; gray) and runt (magenta). The midline shows evidence of twisting (arrowheads; compare to A and B). Scale bar, 50 μ m. (E) *scb* mRNA in fixed wild-type (top) and *trk2/trk3* (bottom) embryos. Embryos were co-stained with Runt and *scb* (magenta) and Runt alone (green). (F) Distribution of right- versus left-handed twisting in *ksr RNAi* embryos. Left: an example of right- (R) and left (L)-handed twisting with the midline highlighted in purple. Anterior is up and posterior is down. Right: the difference between left and right handedness is not statistically significant ($n = 24$, $p = 0.83$, binomial test). Other genotypes associated with twisting are depicted in Table S1. Development of a wild-type embryo is shown in Video S1. Comparison of wild type, *trk2/trk3*, *ksr RNAi*, and *egfr* mutant embryos under oil is presented in Video S3.

the anterior and posterior poles of the embryo at very early stages of development.¹⁴ The other is through activation of EGFR, primarily in a lateral stripe during cellularization¹⁵ (Figure 1C). To establish which of these instances of signaling is responsible for this twisting effect, we observed embryos from transheterozygous maternal mutants for the Torso ligand Trunk (*trk2/trk3*; both protein nulls) or zygotic mutants of EGFR (*EGFR^{2w74}/EGFR^{CO}*; hypomorph and null, respectively) using phase contrast microscopy. We used zygotic EGFR mutants because germline clones were shown not to affect embryonic development.¹⁶ Trunk mutants recapitulated the twisting found in *ksr RNAi* embryos, while EGFR mutants did not¹⁶ (Figure 1D; Video S3; Table S1). These results show that terminal patterning, through the Torso receptor, specifies mechanisms that maintain bilateral symmetry during body axis elongation.

Embryos that harbor a mutation in the alpha integrin Scab (*scb*) have also been found to twist during gastrulation¹² (Table S1), so we investigated whether this effect is also dependent on terminal patterning. We performed *in situ* hybridization against *scb* mRNA and found that in wild-type embryos the

mRNA was localized in an arrow shape at the posterior dorsal area of the embryo, consistent with previous findings¹⁷ (Figure 1E, top). This expression was completely absent in our *trk* mutants (Figure 1E, bottom); therefore, expression of *scb* is downstream of the terminal patterning system.

Overall, our results uncover a previously undescribed role for the downstream components of terminal patterning, in maintaining bilateral symmetry during extension. Specifically, they suggest that terminal patterning plays a role in specifying factors crucial for maintaining bilateral symmetry during morphogenesis in addition to its well-established role in determining cell fates and behaviors at the anterior and posterior poles³ and aiding the convergent extension process by orienting T1 transitions.^{18–20}

Midline extension dynamics in twisting embryos indicate a buckling instability

We hypothesized that the twisting phenotype in terminal patterning knockdowns was the result of stochastic fluctuations rather than a mispatterning of active force generation.

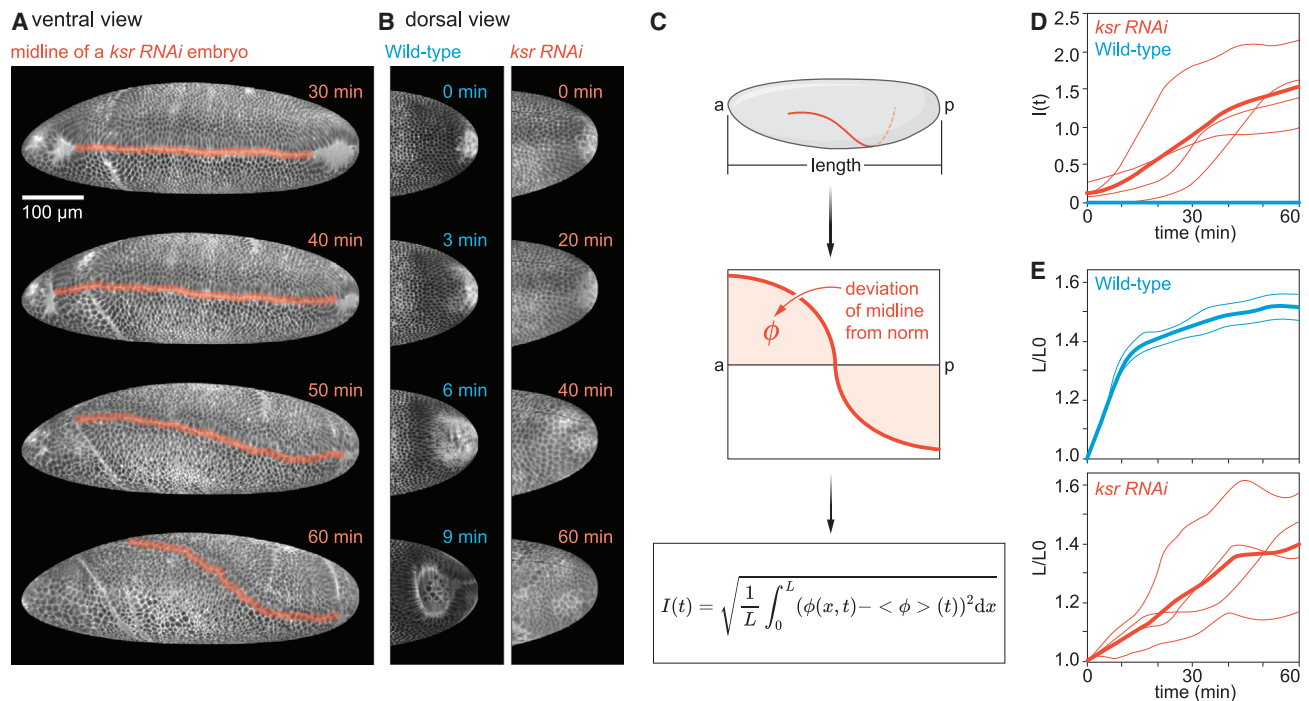


Figure 2. Reduced Ras signaling causes loss of symmetry during body axis extension

(A) Light sheet movie of a *ksr RNAi* embryo (midline highlighted in orange). The start of ventral furrow formation is $t = 0$. Midline twisting occurs with the start of tissue extension. Scale bar, 100 μm .
 (B) PMG formation is disrupted (right) compared to wild type (left). Different time scales were chosen to account for potential differences in developmental time.
 (C) Schematic of RMSD of the midline (STAR Methods).
 (D) RMSD of midline position in *ksr RNAi* (orange) and wild-type (blue) embryos over time. Individual embryos are shown as single traces; averages are bold lines.
 (E) Length of midline in wild-type (blue, top) and *ksr RNAi* (orange, bottom) embryos over time. Each trace is from one embryo, and the bold trace is the average. A *ksr RNAi* embryo is also shown in Video S2.

To test this hypothesis, we determined the number of left-versus right-handed twists in *ksr RNAi* embryos (chosen for their experimental tractability). A previous study found that *ksr RNAi* embryos contain no detectable levels of ERK phosphorylation at the embryonic poles, and that they otherwise recapitulate phenotypes associated with strong loss of terminal patterning, though downstream targets are not as heavily affected as they are in *trk* mutants¹³ (data not shown). We found that left and right chirality occur with similar frequencies (Figure 1F; left = 13 embryos, right = 11 embryos, $p = 0.83$, binomial test), indicating that the direction of twisting is not biased.

Imaging *ksr RNAi* embryos expressing a membrane marker revealed that twisting begins after the ventral midline has formed (just after ventral furrow formation) and as the fast phase of germband extension is occurring (Figure 2A; Video S2). Prior to twisting, inadequate PMG formation was the only observable defect, consistent with KSR's role in the terminal patterning system^{3,13} (Figure 2B).

Taken together, the timing of the onset of twisting (during extension), the loss of PMG formation, and the stochastic direction of twisting reminded us of a compressed rod in a tubular confinement (such as an underground drill).^{21,22} When compressed on either side, the rod experiences a buckling instability that causes a helical twist.²¹ The direction of the helix is sensitive to torque.²² Given this model, we hypothesized the following

mechanism for twisting during extension: extension on both lateral sides of the embryo occurs through terminal patterning-independent cell behaviors, but without proper PMG formation and movement this tissue has no room to grow, increasing mechanical stress and creating a buckling instability. Because the system is unstable, any small fluctuation in left-right symmetry, due to things like potential differences in lateral extension rates or slight asymmetries in invagination, could cause the growing tissue to twist into a helix as it relieves stress. The random direction of twisting that we observed in our embryos supports this model, as stochastically generated torque on either the right or left would dictate the direction of the helical twist in this unstable regime.

To begin to test this model, we calculated velocity fields of tissue flow on the embryo surface, using tissue cartography of our light-sheet movies and particle image velocimetry.^{23,24} Tissue cartography is a method by which the surface of the 3D embryo is projected into 2D, similar to the projection of a globe into a map.²³ First, we tracked the midline position by manually annotating the midline at one time point, then evolved this position over time using the calculated velocity fields. To quantify midline twisting, we found the deviation of the midline from a straight line (Figure 2C). From the cartographic surface projections, we found the midline position along the DV axis, characterized by azimuthal angle ϕ . The midline remains straight (ϕ is constant along embryo length) for the wild type, whereas *ksr RNAi*

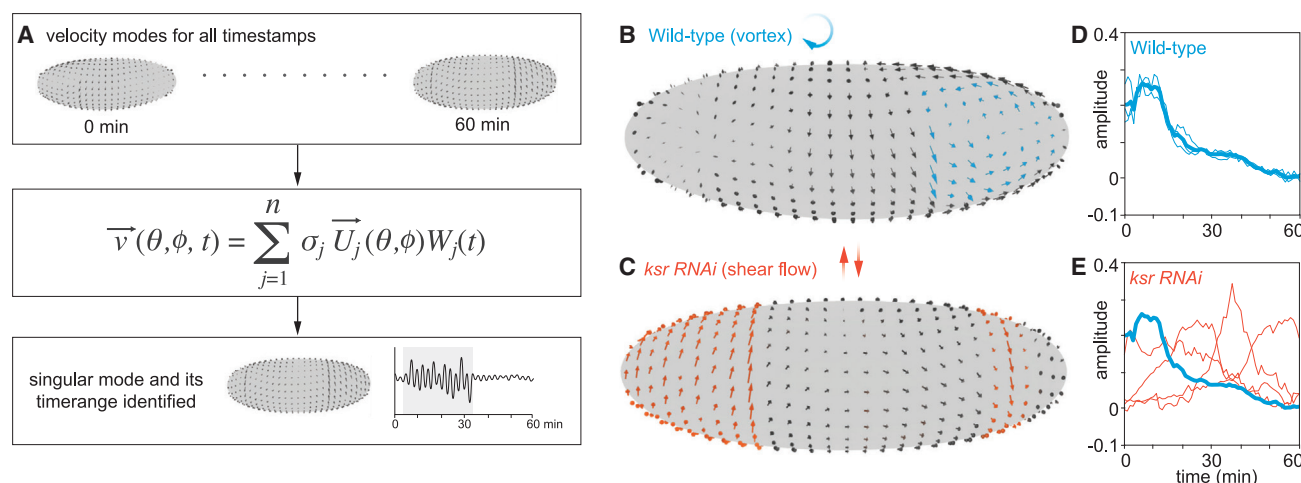


Figure 3. Reduced Ras signaling globally restructures tissue flows

(A) Schematic of singular value decomposition (SVD; STAR Methods).

(B and C) SVD of wild-type (B) and *ksr RNAi* (C) embryos. Image is a representative embryo with its primary velocity mode shown at a time when this mode is most prevalent. Velocity arrows are colored to depict the vortex (B, blue) and shear flow (C, orange) prevalent in the stationary modes.

(D and E) Time-dependent amplitudes of the first mode (the times when the mode contributes most to the overall motion of the tissue) for wild-type (D) and *ksr RNAi* (E) embryos. The bold lines depict the wild-type average for comparison. Each non-bold line is a trace of an individual embryo. Other embryo modes are shown in Figure S1 along with the fraction of variance described by the modes.

embryos twist considerably (ϕ has large variation over the embryo length) at the end of convergent extension (Figure 2C, top and middle). We quantified the net twisting $I(t)$ at a given time as the root-mean-squared deviation (RMSD) of the midline from a straight line, given by the equation:

$$I(t) = \sqrt{\frac{1}{L} \int_0^L (\phi(x, t) - \langle \phi \rangle(t))^2 dx},$$

where $\langle \phi \rangle(t)$ is the mean of the midline position along the midline (Figure 2C, middle and bottom). If a large twist occurs, $\phi(x, t)$ will be large, as will $I(t)$. If $\phi(x, t)$ is close to 0, as for a straight line, $I(t)$ will also be close to 0.

In a model of buckling instability, the dynamics of twisting are expected to reflect an initial lag phase when stress is increasing, then an increasing deviation from a straight line until stress is relieved and extension stops. Indeed, $I(t)$ lagged from 0 to around 20 min, peaked at ~30 min, but slowed after ~40 min, showing twisting mainly occurs in a short window and levels off otherwise (Figure 2D). Furthermore, the length of the extending midline in *ksr RNAi* embryos reflected a delay in extension compared to wild type: wild-type midlines extended fastest at the onset of gastrulation and slowed over time, consistent with the reported “fast” and “slow” phases of germband extension (Figure 2E, top). In the *ksr RNAi* background, the midline extension was slow at first, then underwent a period of dramatic extension before slowing again (Figure 2E, bottom). Additionally, wild-type midline extension was much more stereotyped between embryos than in *ksr RNAi* embryos. Altogether these results support the idea of instability leading to a helical twist when terminal patterning and downstream morphogenesis are disrupted.

Global tissue flows support a model of buckling instability

Thus far, our quantifications have focused on the midline as an approximation of tissue flow. Next, we extended our analysis to global tissue flows, including movement of the lateral germband. Do the changes to global morphogenetic movements in *ksr RNAi* embryos also indicate a buckling instability? To answer this, we decomposed the time-dependent velocity field on the surface of the embryo as sums of products of spatial and temporal modes using singular value decomposition (SVD; Figure 3A).²⁵ We chose this technique because it allows us to focus on specific modes of motion and treats the embryo as a global tissue, rather than PIV, which only analyzes individual velocity vectors, not patterns. The first dominant mode is able to capture a significant amount of variance both in the wild type and the *ksr RNAi* embryos (Figure S1). In the wild type, the principal velocity mode formed a vortex at the lateral posterior end of the embryo, consistent with tissue flow during germband extension²⁶ (Figures 3B and S1). The amplitude of this mode peaked between 5 and 20 min after ventral furrow formation, again consistent with the time period of germband extension, and this time dependence was highly similar across all 3 measured embryos (Figure 3D). In the *ksr RNAi*, the velocity field showed signs of shear flow, with vectors on either pole pointing opposite one another. This, the twisting motion itself, became the principal velocity mode (Figures 3C and S1). Additionally, the time dependence of this velocity mode was highly varied between samples and was delayed compared to the principal velocity mode in the wild type (Figure 3E). Overall, these quantifications show that although the body axis extends in *ksr RNAi* and in wild-type backgrounds, the extension during twisting in *ksr RNAi* embryos is delayed and more variable compared to the mostly planar extension of wild-type embryos, consistent with buckling.

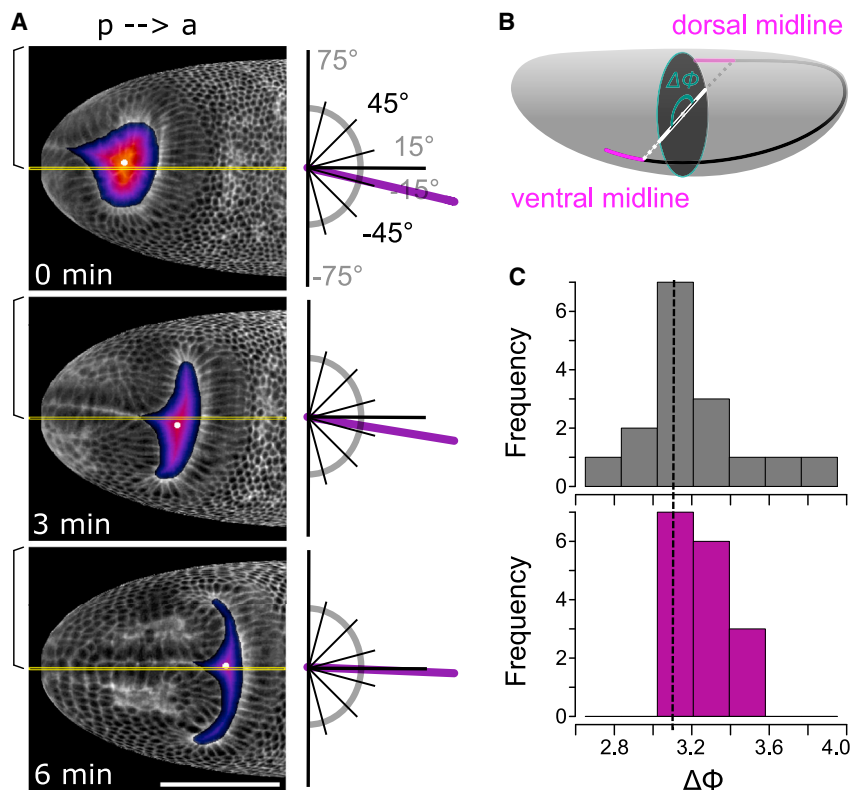


Figure 4. Dynamic reduction of fluctuating asymmetry in wild-type embryos

(A) Example of fluctuating asymmetry during tissue extension. Left: white dot shows the center of the PMG invagination. The yellow line is the middle of the embryo determined by geometry and lies parallel to the AP axis. Note the fluctuations of the dot around the middle. Right: the angle of the midline (degrees), from its posterior-most point to the PMG central dot. This angle would be expected to be 0° for a perfectly left-right symmetric embryo.

(B) Schematic of midline angle. Midline deviation is measured as the difference in angle $\Delta\Phi$ (circumference around the DV axis, inset) between the dorsal and ventral midline. Without fluctuation, this difference would be expected to be 3.14 (π) radians. See also Video S4.

(C) Histogram of $\Delta\Phi$ measurements for 16 embryos at 0 min (gray) and 60 min (purple) after the midline becomes visible on the dorsal side. The distribution decreases significantly between these two time points ($p = 0.0002$, F-test). The black dotted line marks 3.14 radians. Related data are presented in Figure S2. Genotypes potentially correlated with reduction of fluctuating asymmetry are shown in Figure S3.

Torsion is corrected during body axis extension in wild-type embryos

Helical buckling is highly sensitive to torque.²² Although it is difficult to directly measure the initial torque in twisting embryos, we questioned whether we could observe any signs of it in wild-type embryos. The genetic specification and morphogenetic processes leading to germband elongation are presumed to be laterally symmetrical, leading to highly stereotypical extension parallel to the AP axis.⁹ However, we questioned whether intrinsic stochastic variation in the processes that drive body axis extension (i.e., rate of cell intercalations or folding/invagination events) could create left or right torsion. Using light sheet microscopy, we imaged wild-type embryos expressing a membrane marker (Resille:GFP) throughout the process of axis extension. Manually tracing the PMG invagination of a single embryo, we found slight LR variations throughout germband elongation (Figure 4A; Video S4). To determine if this was a common effect, we compared the positions of the dorsal and ventral midline in a sample of embryos (Figures 4B and S2; STAR Methods). If the tissue were extending parallel to the AP axis of the embryo, we would expect the average angle between dorsal and ventral midlines ($\Delta\Phi$) to be exactly π radians (180 deg.). Taking a single time point during body axis extension when the midline was first apparent on the dorsal side, we found a distribution of $\Delta\Phi$ that ranged from 2.65 to 3.94 radians (Figure 4C, top; median = 3.18 and SD = 0.31, $n = 16$). Finally, we tested whether this asymmetry persists throughout gastrulation. We repeated this measurement at a time point 60 min later and found that the range of $\Delta\Phi$ decreased to 3.11–3.47 radians (Figure 4C,

bottom; median = 3.23 and SD = 0.11). This decrease in variance was statistically significant ($p = 0.0002$, F-test, $n = 16$). Overall, these data indicate that torsion present during the early stages of germband extension is corrected over time in wild-type embryos.

Integrin attachment is a possible mechanism for suppressing torsion

Given these results, we propose the following model: bilaterally stable germband extension occurs when the PMG is able to invaginate and move anteriorly to make room for the extending tissue, and this smooth motion buffers any bilaterally asymmetrical noise. When PMG movement is disrupted, as it is in terminal patterning mutants, the increased mechanical stress from the extending germband creates an instability, such that small asymmetries can derail the proper tissue flow and cause catastrophic twists.

When terminal patterning is disrupted, both midline elongation and global tissue flows are delayed compared to wild type, which supports the idea of a build-up of mechanical stress. Additionally, we found increased variability in the timing of tissue movement and midline extension in the KSR knockdown embryos, which is indicative of instability. Finally, we observe fluctuating asymmetries in wild-type embryos and see that the direction of twisting in *ksr RNAi* embryos is random. These observations support the idea that random noise in body axis extension, invaginations, or mechanical properties of the tissue could be the root of bilateral asymmetry in terminal patterning mutants.

Previous studies have correlated loss of the PMG with a “folded gastrulation” phenotype, where ectopic folds occur in the germband, presumably due to an increase of mechanical stress.^{27,28} We expect that the difference between twisting and folding may have to do with the function of the integrin Scab (encoded by the gene *scb*). Scab has been implicated in the second phase of PMG formation, where the PMG invagination moves toward the anterior of the embryo.¹⁰ Scab is proposed to anchor the embryo to the outer vitelline membrane, to provide traction for the moving tissue.^{10,12} Furthermore, it has recently been shown that *scb* is not important for the initial phases of PMG formation,²⁹ which correlates with when we find the highest degree of asymmetry in wild-type embryos (Figure 4C). Regarding our model and previous results,¹² it could be that the friction force provided by this integrin attachment is suppressing torsion. We therefore expect genotypes resulting in loss of *scb* (i.e., loss of traction) would correlate more with a twisting phenotype, while embryos with intact *scb* but disrupted PMG formation would preferentially buckle. We do find that embryos from *trk* mutant mothers, where *scb* expression is ablated (Figure 1E), twist frequently, while zygotic *fog* mutant embryos, where *scb* expression is intact (STAR Methods) but PMG formation is disrupted, tend to buckle/fold (Figure S3). Overexpression of *scb* causes a folding phenotype that is similar to *fog*^{RA67} embryos, except that PMG invagination is still present (Figure S3). Finally, although *ksr RNAi* embryos twist, when *scb* was overexpressed in a *ksr RNAi* background the embryos folded (Figure S3). Interestingly, although the expression pattern of *scb* seems to be mildly disrupted in *ksr RNAi* backgrounds, expression is not completely ablated (Figure S3). However, we believe that the sensitivity of our assays and analysis is currently unable to capture *scb* disruption in this background. The twisting and buckling phenotypes seem to be related, as we did occasionally find both phenotypes in a given genotype. We hypothesize that built-up stress is relaxed in whichever way is most energetically favorable to the embryo—while complex individual circumstances can affect this, the proclivity of a genotype for either twisting or folding does seem to correlate with *scb* expression. However, the expression, distribution, and function of Scab protein itself and its necessary binding partners during *Drosophila* gastrulation and PMG movement remain unknown.

Our results show that there are small fluctuating asymmetries in normally developing embryos, that these variabilities are highest at the beginning of germband extension, and that they decrease over time. Fluctuating asymmetries could be caused by differences in convergence and extension rates on one lateral side of the embryo compared to the other,³⁰ left/right differences in PMG invagination, or factors relating to midline elasticity or material properties of the tissue. Because it is difficult to disentangle which factors could cause twisting in mutants (and which are secondary effects of twisting), we are not able to directly compare these wild-type results to mutants; nevertheless, these results support a model in which small, tissue-intrinsic sources of torque are present and are suppressed over time, and we expect that this suppression mechanism is related to the inability of terminal patterning mutants to maintain symmetry. Additionally, although the measured left-right variability is small (for example, the range of the distribution at 0 min was 2.65–3.94 radians), this difference in angle could cause significant

downstream effects after full extension, if it were not actively corrected. As discussed elsewhere, the embryos accounting for a small degree of left-right variability could indicate developmental robustness to external perturbations or internal developmental errors.^{31–33} Previously described mechanisms to buffer noise in development have found that supercellular networks tend to filter out noise.^{31–33} Our results support this paradigm and extend it to whole-embryo tissue flows. In the future, it will be interesting to compare the mechanisms for preserving bilateral symmetry in *Drosophila* to other organisms that preserve symmetry, like somites in zebrafish³² and the primitive streak in amniotes,³⁴ and against organisms that require symmetry breaking for elongation such as *C. elegans*.³⁵

STAR★METHODS

Detailed methods are provided in the online version of this paper and include the following:

- KEY RESOURCES TABLE
- RESOURCE AVAILABILITY
 - Lead contact
 - Materials availability
 - Data and code availability
- EXPERIMENTAL MODEL AND SUBJECT DETAILS
 - Fly stocks and embryo preparation
- METHOD DETAILS
 - Fly stocks and genetics
 - Analysis of EGFR mutants
 - Fixation and antibody staining
 - RNA probe generation and *in situ* hybridization
 - Fixed imaging
 - *scab* mRNA analysis
 - Scab overexpression line validation
 - Light sheet imaging
 - Particle image velocimetry (PIV)
 - Low dimensional representation of 4D live imaging data
 - Midline tracking and quantifications
 - Dorsal and ventral midline angle analysis
- QUANTIFICATION AND STATISTICAL ANALYSIS

SUPPLEMENTAL INFORMATION

Supplemental information can be found online at <https://doi.org/10.1016/j.cub.2023.07.050>.

ACKNOWLEDGMENTS

Research reported in this publication was supported by NIGMS of the NIH under grant number T32GM007388 (to Princeton Molecular Biology) and NIH Research Grant RO1GM134204 (to S.Y.S.). We would like to thank Gary Laevsky and the Confocal Imaging Facility, a Nikon Center of Excellence, in the Department of Molecular Biology at Princeton University for instrument use and technical advice. Additionally, we would like to thank Lucy Reading-Ikkanda for figure design, Eric Wieschaus and Trudi Schüpbach for reagents and helpful comments, and members of the Streichan lab, as well as past and present members of the Shvartsman lab at Princeton and at the Flatiron Institute for useful feedback and discussions. Stocks obtained from the Bloomington *Drosophila* Stock Center (NIH P40OD018537) were used in this study.

AUTHOR CONTRIBUTIONS

C.M.S. performed experiments and wrote the manuscript. S.D. performed computational analysis of experimental data. V.J.-S. contributed code for analysis of left-right fluctuations in Figure 4. S.J.S. advised on analysis and experimental design. S.Y.S. advised on analysis and experimental design, procured funding for the research, and advised on manuscript writing. All authors helped review the manuscript.

DECLARATION OF INTERESTS

The authors declare no competing interests.

Received: September 29, 2022

Revised: June 29, 2023

Accepted: July 24, 2023

Published: August 9, 2023

REFERENCES

- Genikhovich, G., and Technau, U. (2017). On the evolution of bilaterality. *Development* 144, 3392–3404. <https://doi.org/10.1242/dev.141507>.
- Grimes, D.T. (2019). Making and breaking symmetry in development, growth and disease. *Development* 146, dev170985. <https://doi.org/10.1242/dev.170985>.
- Smits, C.M., and Shvartsman, S.Y. (2020). Chapter six—The design and logic of terminal patterning in *Drosophila*. In *Current Topics in Developmental Biology*, 137, S. Small, and J. Briscoe, eds. (Academic Press), pp. 193–217. <https://doi.org/10.1016/bs.ctdb.2019.11.008>.
- Kong, D., Wolf, F., and Großhans, J. (2017). Forces directing germ-band extension in *Drosophila* embryos. *Mech. Dev.* 144, 11–22. <https://doi.org/10.1016/j.mod.2016.12.001>.
- Perkins, L.A., Larsen, I., and Perrimon, N. (1992). Corkscrew encodes a putative protein tyrosine phosphatase that functions to transduce the terminal signal from the receptor tyrosine kinase torso. *Cell* 70, 225–236. [https://doi.org/10.1016/0092-8674\(92\)90098-W](https://doi.org/10.1016/0092-8674(92)90098-W).
- Schlopp, A.E., Bandodkar, P.U., and Reeves, G.T. (2020). Chapter five—Formation, interpretation, and regulation of the *Drosophila* Dorsal/NF- κ B gradient. In *Current Topics in Developmental Biology*, 137, S. Small, and J. Briscoe, eds. (Academic Press), pp. 143–191. <https://doi.org/10.1016/bs.ctdb.2019.11.007>.
- Tran, H., Walczak, A.M., and Dostatni, N. (2020). Chapter four—Constraints and limitations on the transcriptional response downstream of the Bicoid morphogen gradient. In *Current Topics in Developmental Biology*, 137, S. Small, and J. Briscoe, eds. (Academic Press), pp. 119–142. <https://doi.org/10.1016/bs.ctdb.2019.12.002>.
- Gilmour, D., Rembold, M., and Leptin, M. (2017). From morphogen to morphogenesis and back. *Nature* 541, 311–320. <https://doi.org/10.1038/nature21348>.
- Mitchell, N.P., Lefebvre, M.F., Jain-Sharma, V., Claussen, N., Raich, M.K., Gustafson, H.J., Bausch, A.R., and Streichan, S.J. (2022). Morphodynamic atlas for *Drosophila* development. Preprint at bioRxiv. <https://doi.org/10.1101/2022.05.26.493584>.
- Baillies, A., Collinet, C., Philippe, J.-M., Lenne, P.-F., Munro, E., and Lecuit, T. (2019). Genetic induction and mechanochemical propagation of a morphogenetic wave. *Nature* 572, 467–473. <https://doi.org/10.1038/s41586-019-1492-9>.
- Manning, A.J., Peters, K.A., Peifer, M., and Rogers, S.L. (2013). Regulation of epithelial morphogenesis by the G protein-coupled receptor Mist and its ligand Fog. *Sci. Signal.* 6, ra98. <https://doi.org/10.1126/scisignal.2004427>.
- Münster, S., Jain, A., Mietke, A., Pavlopoulos, A., Grill, S.W., and Tomancak, P. (2019). Attachment of the blastoderm to the vitelline envelope affects gastrulation of insects. *Nature* 568, 395–399. <https://doi.org/10.1038/s41586-019-1044-3>.
- Marmion, R.A., Yang, L., Goyal, Y., Jindal, G.A., Wetzel, J.L., Singh, M., Schüpbach, T., and Shvartsman, S.Y. (2021). Molecular mechanisms underlying cellular effects of human MEK1 mutations. *Mol. Biol. Cell* 32, 974–983. <https://doi.org/10.1091/mbc.E20-10-0625>.
- Gabay, L., Seger, R., and Shilo, B.-Z. (1997). In situ activation pattern of *Drosophila* EGF receptor pathway during development. *Science* 277, 1103–1106. <https://doi.org/10.1126/science.277.5329.1103>.
- Lim, B., Dsilva, C.J., Levario, T.J., Lu, H., Schüpbach, T., Kevrekidis, I.G., and Shvartsman, S.Y. (2015). Dynamics of inductive ERK signaling in the *Drosophila* embryo. *Curr. Biol.* 25, 1784–1790. <https://doi.org/10.1016/j.cub.2015.05.039>.
- Clifford, R., and Schüpbach, T. (1992). The torpedo (DER) receptor tyrosine kinase is required at multiple times during *Drosophila* embryogenesis. *Development* 115, 853–872. <https://doi.org/10.1242/dev.115.3.853>.
- Stark, K.A., Yee, G.H., Roote, C.E., Williams, E.L., Zusman, S., and Hynes, R.O. (1997). A novel alpha integrin subunit associates with betaPS and functions in tissue morphogenesis and movement during *Drosophila* development. *Development* 124, 4583–4594. <https://doi.org/10.1242/dev.124.22.4583>.
- Collinet, C., Rauzi, M., Lenne, P.-F., and Lecuit, T. (2015). Local and tissue-scale forces drive oriented junction growth during tissue extension. *Nat. Cell Biol.* 17, 1247–1258. <https://doi.org/10.1038/ncb3226>.
- Lye, C.M., Blanchard, G.B., Naylor, H.W., Muresan, L., Huisken, J., Adams, R.J., and Sanson, B. (2015). Mechanical coupling between endoderm invagination and axis extension in *Drosophila*. *PLoS Biol.* 13, e1002292. <https://doi.org/10.1371/journal.pbio.1002292>.
- Rauzi, M., Krzic, U., Saunders, T.E., Krajnc, M., Zihler, P., Hufnagel, L., and Leptin, M. (2015). Embryo-scale tissue mechanics during *Drosophila* gastrulation movements. *Nat. Commun.* 6, 8677. <https://doi.org/10.1038/ncomms9677>.
- Gao, D.-L., and Huang, W.-J. (2015). A review of down-hole tubular string buckling in well engineering. *Pet. Sci.* 12, 443–457. <https://doi.org/10.1007/s12182-015-0031-z>.
- Huang, W., Gao, D., Wei, S., and Chen, P. (2015). Boundary conditions: a key factor in tubular-string buckling. *SPE J.* 20, 1409–1420. <https://doi.org/10.2118/174087-PA>.
- Heemskerk, I., and Streichan, S.J. (2015). Tissue cartography: compressing bio-image data by dimensional reduction. *Nat. Methods* 12, 1139–1142. <https://doi.org/10.1038/nmeth.3648>.
- Thielicke, W., and Sonntag, R. (2021). Particle image velocimetry for MATLAB: accuracy and enhanced algorithms in PIVlab. *J. Open Res. Softw.* 9, 12. <https://doi.org/10.5334/jors.334>.
- Dutta, S., Djabrayan, N.J.-V., Smits, C.M., Rowley, C.W., and Shvartsman, S.Y. (2020). Excess dNTPs trigger oscillatory surface flow in the early *Drosophila* embryo. *Biophys. J.* 118, 2349–2353. <https://doi.org/10.1016/j.bpj.2020.03.010>.
- Streichan, S.J., Lefebvre, M.F., Noll, N., Wieschaus, E.F., and Shraiman, B.I. (2018). Global morphogenetic flow is accurately predicted by the spatial distribution of myosin motors. *eLife* 7, e27454. <https://doi.org/10.7554/eLife.27454>.
- Parks, S., and Wieschaus, E. (1991). The *Drosophila* gastrulation gene *concertina* encodes a G α -like protein. *Cell* 64, 447–458. [https://doi.org/10.1016/0092-8674\(91\)90652-F](https://doi.org/10.1016/0092-8674(91)90652-F).
- Zusman, S.B., and Wieschaus, E.F. (1985). Requirements for zygotic gene activity during gastrulation in *Drosophila melanogaster*. *Dev. Biol.* 111, 359–371. [https://doi.org/10.1016/0012-1606\(85\)90490-7](https://doi.org/10.1016/0012-1606(85)90490-7).
- Gehrels, E.W., Chakraborty, B., Perrin, M.-E., Merkel, M., and Lecuit, T. (2023). Curvature gradient drives polarized tissue flow in the *Drosophila* embryo. *Proc. Natl. Acad. Sci. USA* 120, e2214205120. <https://doi.org/10.1073/pnas.2214205120>.
- Stern, T., Shvartsman, S.Y., and Wieschaus, E.F. (2022). Deconstructing gastrulation at single-cell resolution. *Curr. Biol.* 32, 1861–1868.e7. <https://doi.org/10.1016/j.cub.2022.02.059>.

31. Eritano, A.S., Bromley, C.L., Bolea Albero, A., Schütz, L., Wen, F.-L., Takeda, M., Fukaya, T., Sami, M.M., Shibata, T., Lemke, S., and Wang, Y.-C. (2020). Tissue-scale mechanical coupling reduces morphogenetic noise to ensure precision during epithelial folding. *Dev. Cell* 53, 212–228.e12. <https://doi.org/10.1016/j.devcel.2020.02.012>.
32. Naganathan, S.R., Popović, M., and Oates, A.C. (2022). Left–right symmetry of zebrafish embryos requires somite surface tension. *Nature* 605, 7910. <https://doi.org/10.1038/s41586-022-04646-9>.
33. Yevick, H.G., Miller, P.W., Dunkel, J., and Martin, A.C. (2019). Structural redundancy in supracellular actomyosin networks enables robust tissue folding. *Dev. Cell* 50, 586–598.e3. <https://doi.org/10.1016/j.devcel.2019.06.015>.
34. Asai, R., Prakash, V.N., Sinha, S., Prakash, M., and Mikawa, T. (2023). Coupling and uncoupling of midline morphogenesis and cell flow in amniote gastrulation. Preprint at bioRxiv. <https://doi.org/10.1101/2023.05.26.542486>.
35. Priess, J.R., and Hirsh, D.I. (1986). *Caenorhabditis elegans* morphogenesis: the role of the cytoskeleton in elongation of the embryo. *Dev. Biol.* 117, 156–173. [https://doi.org/10.1016/0012-1606\(86\)90358-1](https://doi.org/10.1016/0012-1606(86)90358-1).
36. Potter, C.J., and Luo, L. (2010). Splinkerette PCR for mapping transposable elements in *Drosophila*. *PLoS One* 5, e10168. <https://doi.org/10.1371/journal.pone.0010168>.
37. Schindelin, J., Arganda-Carreras, I., Frise, E., Kaynig, V., Longair, M., Pietzsch, T., Preibisch, S., Rueden, C., Saalfeld, S., Schmid, B., et al. (2012). Fiji: an open-source platform for biological-image analysis. *Nat. Methods* 9, 676–682. <https://doi.org/10.1038/nmeth.2019>.
38. Rørth, P. (1996). A modular misexpression screen in *Drosophila* detecting tissue-specific phenotypes. *Proc. Natl. Acad. Sci. USA* 93, 12418–12422. <https://doi.org/10.1073/pnas.93.22.12418>.
39. Müller, H.A.J. (2008). Immunolabelling of embryos. *Methods Mol. Biol.* 420, 207–218. https://doi.org/10.1007/978-1-59745-583-1_12.
40. Kosman, D., Mizutani, C.M., Lemons, D., Cox, W.G., McGinnis, W., and Bier, E. (2004). Multiplex detection of RNA expression in *Drosophila* embryos. *Science* 305, 846. <https://doi.org/10.1126/science.1099247>.
41. Gramates, L.S., Agapite, J., Attrill, H., Calvi, B.R., Crosby, M.A., dos Santos, G., Goodman, J.L., Goutte-Gattat, D., Jenkins, V.K., Kaufman, T., et al. (2022). FlyBase: a guided tour of highlighted features. *Genetics* 220, iyac035. <https://doi.org/10.1093/genetics/iyac035>.

STAR★METHODS

KEY RESOURCES TABLE

REAGENT or RESOURCE	SOURCE	IDENTIFIER
Antibodies		
Mouse anti-Neurotactin	DSHB	RRID: AB_528404
Guinea pig anti-Runt	Wieschaus lab	N/A
Donkey anti-mouse, Alexa 568	Thermo Fisher Scientific	RRID: AB_2534013
Goat anti-guinea pig, Alexa 488	Thermo Fisher Scientific	RRID: AB_2534117
Sheep anti-DIG	Roche	RRID: AB_514496
Donkey anti-sheep, Alexa 568	Thermo Fisher Scientific	RRID: AB_2535753
Chemicals, peptides, and recombinant proteins		
T4 DNA Ligase	NEB	M0202S5
Q5 high fidelity master mix	NEB	M0492S
Methanol	VWR	BDH1135
37% Formaldehyde solution	Fisher Scientific	F79-1
Heptane	Sigma	32287
PBS	Fisher Scientific	BP2944
Triton X-100	Fisher Scientific	X100
Aqua-Poly/Mount	Polysciences	18606
BSTYI enzyme with recombinant albumin and rCutSmart Buffer	NEB	R0523S
Critical commercial assays		
Quick-DNATM Tissue/Insect Miniprep Kit	Zymo Research	D6016
Deposited data		
Stains for all scab overexpression and fog mutants	Figshare	https://doi.org/10.6084/m9.figshare.23714361
Trk mutant stains	Figshare	https://doi.org/10.6084/m9.figshare.23714340
<i>ksr RNAi</i> stains (gastrulating)	Figshare	https://doi.org/10.6084/m9.figshare.23714331
<i>ksr RNAi</i> stains (for <i>scb mRNA</i>)	Figshare	https://doi.org/10.6084/m9.figshare.23714058
OreR <i>scb mRNA</i> stains	Figshare	https://doi.org/10.6084/m9.figshare.23714007
Experimental models: Organisms/strains		
cn bw trk2 / cyo	Trudi Schüpbach	N/A
cn bw trk3/cyo	Trudi Schüpbach	N/A
UAS > <i>ksr RNAi</i>	Bloomington Stock Center	41598
Resille:GFP	Eric Wieschaus	N/A
Maternal Triple Driver (MTD)	Bloomington Stock Center	31777
EGFR2W74	Trudi Schüpbach	N/A
EGFRCO	Trudi Schüpbach	N/A
fogRA67 / FM7,Ymal106	Eric Wieschaus	N/A
EP2E65	Eric Wieschaus	N/A
P{matalpha4-GAL-VP16}67; P{matalpha4-GAL-VP16}15	Bloomington Stock Center	80361
Oligonucleotides		
<i>scb</i> cDNA primers (to make <i>in situ</i> probes): forward: AGAACGCGGCTACAATTAATACA	This study	N/A
<i>scb</i> cDNA primers (to make <i>in situ</i> probes): reverse: GGATGCGCCCTATAGTGAGT	This study	N/A
Splinkerette: SPLINK-BOT ³⁶ : CGAAGAGTAA CCGTTGCTAGGAGAGACCGTGGCTGAATG AGACTGGTGTGACACTAGTGG	Potter & Luo ³⁶	N/A

(Continued on next page)

Continued

REAGENT or RESOURCE	SOURCE	IDENTIFIER
Splinkerette: SPLINK-GATC-TOP ³⁶ : GATCCC ACTAGTGTCGACACCACTCTCTAATTTTTT TTTCAAAAAA	Potter & Luo ³⁶	N/A
Splinkerette (PCR): SPLNK#1 ³⁶ : CGAAGAGTA ACCGTTGCTAGGAGAGACC	Potter & Luo ³⁶	N/A
Splinkerette (PCR): 3'SPLNK#1 ³⁶ : CACTCAGA CTCAATACGACAC	Potter & Luo ³⁶	N/A
Splinkerette (PCR): SPLNK#2 ³⁶ : GTGGCTGAA TGAGACTGGTGTCGAC	Potter & Luo ³⁶	N/A
Splinkerette (PCR): 3'SPLNK#2 ³⁶ : GGATGTC TCTTGCCGAC	Potter & Luo ³⁶	N/A
Splinkerette (PCR): 5' SPLNK#1-CASPR ³⁶ : ATAGCACACTTCGGCACG	Potter & Luo ³⁶	N/A
Splinkerette (PCR): 5' SPLNK#2-CASPR ³⁶ : ATTCGTCCGCACACAACC	Potter & Luo ³⁶	N/A
Splinkerette (sequencing): 3'SPLNK-SEQ ³⁶ : CGGGACCACCTTATG	Potter & Luo ³⁶	N/A
Splinkerette (sequencing): 5'SPLNK- CASPR-SEQ ³⁶ : CCTCTCAACAAGCAAACG	Potter & Luo ³⁶	N/A

Recombinant DNA

scb cDNA LP12257	DGRC	Stock 6074; https://dgrc.bio.indiana.edu/stock/6074 ; RRID: DGRC_6074
------------------	------	---

Software and algorithms

Fiji	Schindelin et al. ³⁷	https://imagej.net/software/fiji/ ; RRID: SCR_002285
RStudio	RStudio	https://posit.co/products/open-source/rstudio/ ; RRID: SCR_000432
MATLAB	MathWorks	https://www.mathworks.com/ ; RRID: SCR_001622
Jupyter Notebook	Project Jupyter	https://jupyter.org/
Original code	Github	https://github.com/Shvartsman-Lab/MaintainingSymmetry

RESOURCE AVAILABILITY

Lead contact

Further information and requests for resources and reagents should be directed to the lead contact, Stas Shvartsman (stas@princeton.edu).

Materials availability

Probes for *in situ* hybridization are available from the lead contact upon request. No other unique reagents were generated in this study.

Data and code availability

- Original data that could be deposited within given space limits are deposited on Figshare.
- All original code has been deposited on Github.
- Any additional information required to reanalyze the data reported in this paper is available from the lead contact upon request.

EXPERIMENTAL MODEL AND SUBJECT DETAILS

Fly stocks and embryo preparation

Drosophila melanogaster lines (see [key resources table](#)) were maintained at either 25°C or 18°C. For fixation and immunostaining, embryos were collected on apple juice agar plates for 1-2 h, aged, then dechorionated in bleach. For live imaging, embryos were

either manually dechorionated by rolling around on tape or dechorionated in bleach before mounting. Further details can be found in the [method details](#) section.

METHOD DETAILS

Fly stocks and genetics

For *trk* mutant experiments, *cn bw trk²* / *cyo* flies were crossed to *cn bw trk³* / *cyo* flies (gifts from Trudi Schüpbach), and F1 *cn bw trk²* / *cn bw trk³* (referred to as *trk²/trk³*) females were collected. These females were crossed to any males, and the F2 progeny embryos from these maternal mutants were analyzed.

Resille:GFP; UAS>*ksr RNAi* (Bloomington 41598) was crossed to Maternal Triple Driver (MTD) for all *ksr RNAi* experiments. Resille:GFP; UAS>*ksr RNAi* (Bloomington 41598) with no Gal4 driver were used as control (WT) embryos.

EGFR^{2W74} and *EGFR^{CO}* (Gift of Trudi Schüpbach) were balanced over a GFP marked *cyo* (gift of Amanda Amadeo). 3–6 day old virgin females were crossed to males of the other allele and the F1 embryos were collected for analysis of zygotic EGFR disruption. Previous studies have shown that disrupted maternal EGFR activity does not contribute to the twisting phenotype.¹⁶

fog^{RA67} / FM7, Ymal106 (transcript-null allele) was a gift of Eric Wieschaus.

EP2E65 (*scb* overexpression line) was originally created by Rørth et al.³⁸ and was a gift of Eric Wieschaus.

OreR was used as wild type for fixed imaging experiments and when comparing phenotypes under oil.

Analysis of EGFR mutants

Embryos from the EGFR cross were dechorionated in bleach and aligned on a clean apple juice plate, then imaged on a Nikon Eclipse Ni widefield microscope with a Qi1Mc camera under 488nm light to score for fluorescence. These same embryos were then transferred to a Leica M125 C stereoscope and imaged with a Flexacam C1 camera every minute for 2 or 3 h. Transheterozygous embryos (lacking GFP fluorescence from the balancer) were scored for germband extension defects, none were observed (*n* = 4). *trk²/trk³* and *ksr RNAi* embryos observed with the stereoscope were found to twist. OreR embryos imaged the same way showed similar tissue flows to EGFR transheterozygotes.

Fixation and antibody staining

Embryos for antibody staining were collected for one to 2 h, aged, then dechorionated in bleach. Embryos were heat fixed following a protocol adapted from Müller et al.³⁹: ~5mL 1x TSS solution (4 g/L NaCl, 0.003% Triton X-100 in distilled water) in a scintillation vial was heated in a microwave until hot. A metal mesh net containing the embryos was immersed in the hot TSS and swirled for 10 s. After 10 s, the scintillation vial was placed on ice and immediately filled with ice and cold (4°C) TSS. The scintillation vial was covered with ice and let sit for at least 5 min. The TSS was then decanted and 5mL each of methanol and heptane were added to the embryos in the vial. This was vigorously shaken for ~90 s to remove the vitelline membrane. Devitellinized embryos were transferred to an Eppendorf tube, washed twice with methanol, then stored in methanol at -20°C.

For antibody staining, embryos were rehydrated by stepping into 75%, 50%, then 25% methanol:PBST (phosphate buffered saline + 0.002% Tween) solutions, then washed in 1X PBST. Embryos were then cleared in Image-iT FX signal enhancer (Invitrogen) for 30 min, washed in PBST, and blocked in a 5% Normal Goat Serum (NGS)/10% Bovine Serum Albumin (BSA)/PBST solution for 90 min. After blocking, embryos were washed, then incubated at 4°C overnight in primary antibody solution (1:100 primary antibody, 5% NGS, 1% BSA in PBST). Embryos were then washed, incubated in secondary antibody solution (1:500 Alexa Fluor conjugate, 10% NGS, 1% BSA in PBST) for 90 min, and washed again. Finally, embryos were mounted in Aqua-Poly/Mount (Polysciences) on a coverslip which was sealed with nail polish and stored at 4°C. Primary antibodies used were guinea pig anti-Runt (1:100; gift of Eric Wieschaus), mouse anti-Neurotactin (1:100; Developmental Studies Hybridoma Bank; BP 106).

RNA probe generation and *in situ* hybridization

RNA probes against *scb* mRNA were generated from *scb* cDNA LP12257 (DGRC Stock 6074; <https://dgrc.bio.indiana.edu/stock/6074>; RRID: DGRC_6074). A portion of the *scb* gene was amplified using the following primers:

Forward: AGAACGCGGCTACAATTAATACA

Reverse: GGATGCGCCCTATAGTGAGT

Digoxigenin (DIG) labeled RNA probes against this portion of the *scb* gene were made through an *in vitro* transcription reaction (from the SP6 promoter) which was incubated at 37°C for 3 h then halted by adding DNase and incubating at 37°C for 30 min. RNA was extracted using a Qiagen RNeasy Kit and stored in hybridization buffer at -20°C until use.

For *in situ* hybridization, embryos were prepared as above, but fixed at the interface of heptane and 8% PFA (paraformaldehyde) in PBS (4 mL PBS + 1 mL 37% PFA, 5 mL heptane) by rocking for 20 min. *In situ* hybridization was performed as previously described,⁴⁰ with the following adjustments: we incubated embryos in 80% acetone in PBST at -20°C for 10 min (agitating every few minutes) instead of treating with proteinase K; all hybridization steps were performed at 60°C; probes were denatured at 85°C for 4 min; and secondary antibody staining was performed for 90 min. Primary antibodies used for *in situ* hybridization were: sheep anti-DIG (1:125; Roche #11333089001) and guinea pig anti-Runt (1:100). Secondary antibodies used were Alexa Fluor conjugates (1:500; Invitrogen).

Fixed imaging

Fixed embryos were imaged on a Leica SP5 confocal microscope with HyD detectors. Images were acquired with 20x/NA 0.7 HCX PL APO CS objective using 488 and 561 lasers. Pixel size was $0.76 \times 0.76 \mu\text{m}$ in x and y (pinhole size of 60.69). The z-step varied based on the size of the embryo. To image *scb* in both *trk²/trk³* and wild-type embryos, a z stack through the entire embryo was acquired to ensure that *scb* would be visible if present.

fog^{RA67} zygotic mutant embryos, *ksr RNAi* embryos, and *trk²/trk³* mutant embryos and embryos overexpressing *scb* in a *ksr RNAi* background were heat fixed after germband extension. To get *scb* overexpression in a *ksr RNAi* background, EP2E65 stocks were validated and mapped (see below) and crossed to UAS > *ksr RNAi* lines to create a stable line. These flies were crossed to MTD Gal4 driver females, and the F2 progeny from this cross were fixed and imaged. Embryos were stained for membranes using a Neurotactin antibody (BP106, DSHB). Using a custom Fiji macro, images were mixed and given a random number, so that scoring for phenotypes was blinded. While scoring, each embryo was given a subjective quality score (% out of 100) based on confidence in distinguishing between twisting and folding phenotypes (wild-type phenotypes were excluded because ~75% of *fog^{RA67}* mutants are expected to be heterozygotes and have a wild-type phenotype; difficulties in distinguishing between folding and twisting were mainly due to either poor staining, embryo orientation on the slide, or differences in developmental stage). Only embryos with a 100% quality score were included in the analysis. Results are in Figure S3.

scab mRNA analysis

For *scb* staining, wild-type (OreR) control embryos and *trk²/trk³* embryos at cellularization were mixed in the same Eppendorf tube and therefore treated with the same conditions. Runt staining was used to distinguish wild type (7 runt stripes) from mutants (6 runt stripes) during analysis. *scb* expression was scored blinded to the runt stripe number. Embryos where the number of runt stripes could not be determined were discarded from the analysis. Wild type: $n = 16$; *trk²/trk³*: $n = 16$. All wild-type embryos had observable *scb* expression, while none of the *trk²/trk³* mutants did. Representative embryos are displayed in Figure 1.

To check whether *fog^{RA67}* mutants had disrupted *scb* expression, *fog^{RA67}* zygotic mutants, along with their wild-type siblings, were staged and formaldehyde fixed at nuclear cycle 14/early gastrulation then stained for *scb* mRNA expression. Embryos were imaged sandwiched between two coverslips – for any embryos where *scb* expression was not observed, the coverslips were flipped and the same embryo was imaged on the other side. While wild-type and *fog* mutant embryos could not be distinguished *a priori*, all embryos on the slide were scored and found to express *scb* ($n = 32$). Because *fog^{RA67}* is recessive zygotic lethal on the X chromosome, the percentage of expected *fog* mutant embryos is 25%. Under the hypothesis that *fog* mutants do not express *scb*, we ran a binomial test and found that the observed distribution of *scb* expression (32 of 32 embryos) significantly deviates from the expected distribution (24 of 32; $p = 0.0001$). We therefore concluded that *fog* mutants express *scb*.

Scab overexpression line validation

Scab overexpression flies (EP2E65) were originally generated by Rørth³⁸ and were a gift of Eric Wieschaus. This line was generated by random insertion of a specialized P element into the genome. This P element contains UAS binding sequences and a promoter element, to drive expression when Gal4 is present.

To map the insertion site of the P element in the genome, we used splinkerette PCR mapping.³⁶ This method uses restriction digest of genomic DNA to generate fragments with GATC sticky ends. A specific “splinkerette” oligonucleotide is then ligated to the sticky ends, and PCR is performed using a primer specific to one end of the P element (separate PCRs for both the 5' and 3' ends) and a primer specific to the splinkerette oligonucleotide.

Our splinkerette protocol was adapted from Potter & Luo³⁶ with the following amendments: genomic DNA prep was performed with Quick-DNA (Zymo) kit on 20 male flies, and the gDNA was eluted in 50 μL of DNA elution buffer. The genomic digest was performed with the restriction enzyme BstY1 (NEB) in rCutsmart buffer at 60°C for 2 h, then the enzyme was heat inactivated at 80°C for 20 min. The splinkerette oligonucleotide was then ligated to the gDNA fragments as described, substituting T4 ligase buffer for NEB buffer 2. Two rounds of PCR were performed using Q5 HotStart PCR mastermix. Annealing temperatures were as follows: 63°C for both 3' and 5' PCRs in round 1, 64°C for 3' PCR round 2, and 68°C for 5' PCR round 2.

The resulting product contains a small amount of the P element and some flanking genomic DNA. This was then sequenced and compared to the reference genome of *Drosophila melanogaster*.⁴¹ We found that the P element was inserted in the 5' region of the *scb* gene in the correct orientation to drive *scb* expression. We additionally validated that *scb* mRNA by performing an *in situ* (as described previously) on EP2E65 embryos expressing ubiquitous Gal4 (maternal alpha tubulin 67; 15 driver). We found that *scb* is indeed ubiquitously expressed (data not shown) and that when raised at 18°C the embryos displayed a very “folded” phenotype (Figure S3).

Light sheet imaging

Live light sheet imaging was performed on a Luxendo Multiview (MuVi) SPIM microscope at 22.2x magnification with the following specifications.

Cameras: 2 Hamamatsu C13440 ORCA flash 4.0 cameras
Illumination objectives: 2 Nikon CFI Plan Fluor 10x W 0.3 NA water immersion objectives
Detection objectives: 2 Olympus 20x 1.0 NA water immersion objectives

Laser: 488 nm 40 mW laser set to 5%

Embryos were either dechorionated in bleach or manually dechorionated by rolling around on tape, then mounted in 1-2% low melt agarose solution (melted at 85°C and stored as a liquid at 37°C until use, for no longer than 12 h). Embryos were mounted in a glass capillary tube. The agarose was allowed to harden at room temperature for 2-3 min then pushed with a wire until the embryo was exposed. The wire was cut and the capillary tube was placed on the microscope for imaging.

Images were collected at a frame rate of 1 volume / minute, with exposure times ranging from 50 to 150 ms (depending on the experiment), with the exception of the embryos for [Figures 4C and S2](#), which were collected at a frame rate of 1 volume / 10 min. All images were collected with 2 camera views. Registration and fusion of the left and right camera images was performed using Luxendo's light sheet image processing software. Fused images were downsized by a factor of 2 then converted from Luxendo's output file format (HDF5) to a tag image file format (TIFF) with a bit depth of 8 for further processing and visualization.

Particle image velocimetry (PIV)

To prepare 2D movies for PIV, the membrane channel was inverted such that the middles of cells were white and separated by black lines (to create "particles"). Image lighting was normalized using the "enhance contrast" function in Fiji, using 0.3% as a cutoff for saturated pixels. A mask of the projections was also created using Huang binarization in Fiji. These images were saved as TIFFs with a bit depth of 8 and loaded into the PIVlab GUI in MATLAB²⁴ with 1-2, 2-3 ... sequencing. Settings for image preprocessing were as follows: CLAHE window size = 20px, high-pass kernel size = 15px, intensity capping, Wiener2 Denoise filter window size = 3 px, and auto contrast stretch were all enabled. PIV settings were as follows: algorithm = FFT window deformation, pass 1 interrogation area = 128 px with 64 px step size, pass 2 interrogation area = 64 px with 32 px step size, sub-pixel estimator = Gauss 2x3 point, correlation quality = normal. After PIV was run, post-processing of the vector field was performed to exclude spurious vectors. Velocity limits were manually set to 20 px/frame (corresponding to roughly 11 μm/min, or about 1.5 diameters of a single nucleus) in both u and v directions. The standard deviation filter was set to 3, and missing data interpolation was enabled. Excess vectors out of the image plane were subtracted using the generated mask of the projection. The resultant velocity fields were used for all downstream analysis. Finally, velocity fields were interpolated onto the reconstructed surface of the embryo in 3-dimensions (see below).

Low dimensional representation of 4D live imaging data

To evaluate the velocity-field of the cells on the two-dimensional surface of the embryo from three-dimensional image from light-sheet microscopy, we cartographically project the surface of the embryo on a plane using the software ImSane.²³ This software fits the surface of the embryo, such that each point on the surface is defined by two coordinates (z, ϕ), which translates into cartesian coordinates (X, Y, Z) as

$$X = x_0(z) + R(z)\cos(\phi) \quad \text{Equation 1}$$

$$Y = y_0 + R(z)(1 + \epsilon(z))\sin(\phi)$$

$$Z = z$$

where $\phi \in (-\pi, \pi]$, and $x_0(z)$, $y_0(z)$, $R(z)$, and $\epsilon(z)$ are polynomials of order 4. Next, we project this surface into a 2D plane using the modified proper cylinder coordinate system, where two coordinates are $z'(z)$ and $\phi'(z, \phi)$ defined in Heemskerk and Streichan.²³

We use a particle image velocimetry software PIVLab²⁴ to obtain two-dimensional velocity field $\{v_{z'}, v_{\phi'}\}(z, \phi)$ on this projected map (see [particle image velocimetry](#) section). From the software we export values of $z'(z, \phi)$ and $\phi'(z, \phi)$ in a fine resolution and use interpolation to map the coordinates in $\{z', \phi'\}$ plane to the parameters ($\{z, \phi\}$) and numerically find the corresponding partial derivative. Using this information, we find the local rate of change of the parameters of the projection from this velocity field as:

$$\frac{dz}{dt} = \frac{dz}{dz'} \frac{dz'}{dt} = v_{z'} \frac{dz}{dz'},$$

$$\frac{d\phi}{dt} = \frac{\frac{d\phi'}{dt} - \frac{\partial\phi'}{\partial z} \frac{dz}{dt}}{\frac{\partial\phi'}{\partial\phi}} = \frac{v_{\phi'} - \frac{\partial\phi'}{\partial z} \frac{dz}{dt}}{\frac{\partial\phi'}{\partial\phi}}$$

Next, we calculate two components of velocities $\{v_1, v_2\}$ on the fitted surface similar to polar and azimuthal component of the velocity in a spherical coordinate system defined as:

$$v_1 = \sqrt{\left(\frac{\partial X}{\partial z}\right)^2 + \left(\frac{\partial Y}{\partial z}\right)^2 + \left(\frac{\partial Z}{\partial z}\right)^2} \frac{dz}{dt},$$

$$v_2 = \sqrt{\left(\frac{\partial X}{\partial \phi}\right)^2 + \left(\frac{\partial Y}{\partial \phi}\right)^2 + \left(\frac{\partial Z}{\partial \phi}\right)^2} \frac{d\phi}{dt}$$

Using this algorithm we generate two components of velocity $\{v_1(i, t), v_2(i, t)\}$ for the grid-point i and time t . Next, for each embryo, we assembled a $2m \times T$ dimensional matrix A , in which the $2m$ rows correspond to the two components of velocity (v_1, v_2) at the m grid points and the T columns correspond to the T time frames from the PIV data. Singular Value Decomposition (SVD) of this matrix yields a representation as a sum of rank one matrices²⁵:

$$A = U\Sigma W^T = \sigma_1 U_1 W_1 + \sigma_2 U_2 W_2 + \dots$$

where U_j and W_j denote j th columns of orthogonal matrices U and W , which can be interpreted as the stationary velocity field representing the j th mode and its time-dependent amplitude. The j th element of diagonal matrix Σ , σ_j , corresponds to the magnitude of the j th mode.

Midline tracking and quantifications

We manually identify the position of the midline in the cartographically projected image of the embryo for a given time frame with ~ 1000 points. Then using the velocity-field obtained from PIV on the cartographically projected map, we evolve the position of the points on the midline as a function of time. Next, using the definitions of the cartographic projection (Equation 1) we project back the coordinates of the points defining the midline on the curved surface depicting the embryo. We calculate the length of the midline as a sum of 3D cartesian distance between all the points that define the midline.

Dorsal and ventral midline angle analysis

Embryos were imaged on the light sheet once every 10 min starting at the time when the midline becomes apparent on the dorsal side of the embryo ($n = 16$ embryos). These images were converted to 2D pullbacks as described above. The code for ImSaNE to generate these pullbacks was modified such that left-right handedness is preserved during the 2D mapping.

The dorsal and ventral midlines from “cylinder 1” pullbacks were manually selected with the freehand selection tool in FIJI, then interpolated and smoothed by 1px, and the xy coordinates were exported as a .csv file. The first 90 points were averaged for both the dorsal and ventral midlines, giving two single points. The y-axis of the pullbacks corresponds to the angle phi around the circumference of the embryo, so the yvalue of the ventral point was subtracted from the dorsal point yvalue, and this gives the delta phi value in pixels. To convert to radians, the absolute value of delta phi was multiplied by 2π and divided by the total number of pixels in the image along the phi axis.

For the histograms in Figure 4, the distribution of delta phi from two time points were compared: time $t = 0$ min and time $t = 60$ min. A Shapiro-Wilk normality test was conducted on the distributions from both time points to determine the suitability of statistical tests assuming normality ($p = 0.48$ for $t = 0$ min; $p = 0.09$ for $t = 60$ min; not significant). An F-test was performed to compare the variances between the two time points ($p = 0.0002$), indicating the decreased variance over time is statistically significant.

Manual measurements were performed in FIJI, calculation of delta phi values was performed in MATLAB, and statistical analysis was performed in R.

QUANTIFICATION AND STATISTICAL ANALYSIS

Statistical analysis was performed in R, MATLAB, or Python. Details of the statistical tests performed and resulting p values can be found in figure legends, in the main text, and in the Method Details section. Statistical significance was defined as $p < 0.05$. Strategies to ensure randomization are reported for individual experiments in the Method Details section. Sample size was not estimated prior to analysis. Imaging data were excluded from the analysis if 1) the imaging was not of a high enough quality to confidently classify embryos (bad staining, mistakes in imaging set up, stacks did not capture the necessary range, etc.), 2) the embryos were broken or other artifacts of the fixation and staining procedure were prevalent, or 3) if the embryo could not be confidently classified for any other reason. This was performed while the experimenter was blinded to genotype.